NeuroImage: Clinical 31 (2021) 102737

Contents lists available at ScienceDirect

NeuroImage: Clinical

journal homepage: www.elsevier.com/locate/ynicl

CryptoCEST: A promising tool for spatially resolved identification of fungal brain lesions and their differentiation from brain tumors with MRI

Liesbeth Vanherp [a,1,4], Kristof Govaerts [a,2,4], Matteo Riva [b,c], Jennifer Poelmans [a,3], An Coosemans [b], Katrien Lagrou [d,e], Willy Gsell [a], Greetje Vande Velde [a,5], Uwe Himmelreich [a,5,*]

[a] Biomedical MRI, Department of Imaging and Pathology, KU Leuven, Leuven, Belgium
[b] Laboratory of Tumor Immunology and Immunotherapy, Department of Oncology, Leuven Cancer Institute, KU Leuven, Leuven, Belgium
[c] Department of Neurosurgery, Mont-Godinne Hospital, UCL Namur, Yvoir, Belgium
[d] Laboratory of Clinical Bacteriology and Mycology, Department of Microbiology, Immunology and Transplantation, KU Leuven, Leuven, Belgium
[e] National Reference Centre for Mycosis, Department of Laboratory Medicine, University Hospitals Leuven, Leuven, Belgium

ARTICLE INFO

Keywords:
CEST MR imaging
MR spectroscopy
Fungal infection
Cryptococcosis
Trehalose
Biomarker

ABSTRACT

Infectious brain lesions caused by the pathogenic fungi *Cryptococcus neoformans* and *C. gattii*, also referred to as cryptococcomas, could be diagnosed incorrectly as cystic brain tumors if only based on conventional magnetic resonance (MR) images. Previous MR spectroscopy (MRS) studies showed high local concentrations of the fungal disaccharide trehalose in cryptococcomas. The aim of this study was to detect and localize fungal brain lesions caused by *Cryptococcus* species based on Chemical Exchange Saturation Transfer (CEST) MR imaging of endogenous trehalose, and hereby to distinguish cryptococcomas from gliomas. In phantoms, trehalose and cryptococcal cells generated a concentration-dependent CEST contrast in the 0.2 – 2 ppm chemical shift range, similar to glucose, but approximately twice as strong. *In vivo* single voxel MRS of a murine cryptococcoma model confirmed the presence of trehalose in cryptococcomas, but mainly for lesions that were large enough compared to the size of the MRS voxel. With CEST MRI, combining the more specific CEST signal at 0.7 ppm with the higher signal-to-noise ratio signal at 4 ppm in the CryptoCEST contrast enabled localization and distinction of cryptococcomas from the normal brain and from gliomas, even for lesions smaller than 1 mm^3. Thanks to the high endogenous concentration of the fungal biomarker trehalose in cryptococcal cells, the CryptoCEST contrast allowed identification of cryptococcomas with high spatial resolution and differentiation from gliomas in mice. Furthermore, the CryptoCEST contrast was tested to follow up antifungal treatment of cryptococcomas. Translation of this non-invasive method to the clinic holds potential for improving the differential diagnosis and follow-up of cryptococcal infections in the brain.

1. Introduction

Cryptococcus neoformans and *C. gattii* are the most common causes of fungal brain infection, leading to life-threatening meningoencephalitis and/or localized brain lesions called cryptococcomas (Maziarz and Perfect, 2016; Schwartz et al., 2018). Cryptococcosis mainly affects immunocompromised individuals, yearly resulting in an estimated 223,100 cases in HIV-infected persons worldwide and accounting for 7–10% of the fungal infections reported in solid organ transplant recipients (Beardsley et al., 2019; Rajasingham et al., 2017). In particular *C. gattii* can also cause disease in apparently immunocompetent persons, in whom disease presents most commonly in the form of

Abbreviations: CEST, chemical exchange saturation transfer; CFU, colony forming unit; PBS, phosphate-buffered saline; p.i., post injection; MTR_{asym}, magnetization transfer ratio asymmetry; APT, amide proton transfer; NOE, nuclear Overhauser effect; MRS, magnetic resonance spectroscopy.

* Corresponding author at: Biomedical MRI, Department Imaging and Pathology, KU Leuven, Herestraat 49, O&N1, box 505, 3000 Leuven, Belgium.
E-mail address: uwe.himmelreich@kuleuven.be (U. Himmelreich).
[1] Present addresses: μNEURO Research Centre of Excellence / Imec – Vision Lab, University of Antwerp, Antwerp, Belgium.
[2] SESVanderhave, Tienen, Belgium.
[3] Janssen Pharmaceutica NV, Beerse, Belgium.
[4] L.V. and K.G. contributed equally to this work.
[5] G.V.V. and U.H. contributed equally as last authors.

https://doi.org/10.1016/j.nicl.2021.102737
Received 11 March 2021; Received in revised form 25 May 2021; Accepted 19 June 2021
Available online 24 June 2021

cryptococcomas (Chen et al., 2000; Mitchell et al., 1995). A treatment regimen of several months with the antifungal drugs amphotericin B, flucytosine and/or fluconazole is essential for patient survival, but mortality rates remain high, ranging from 20% in high-income countries to 70% in resource-limited regions (Rajasingham et al., 2017).

Diagnostic imaging, especially MR imaging of the brain, plays an important role in localizing and defining the extent of infection (Charlier et al., 2008). But, conventional MR techniques often lack the specificity to differentiate cryptococcomas from other types of brain lesions (such as cystic brain tumors or abscesses) because most pathological lesions appear as hyperintense lesions on T_2-weighted MR images (Himmelreich and Gupta, 2006). In particular for patients in whom the clinical suspicion for cryptococcosis is low, such as immunocompetent patients, cryptococcomas are initially often incorrectly diagnosed as brain tumors, and the final diagnosis of cryptococcosis is only established after an invasive biopsy or surgical resection of the lesion (Li et al., 2010; Santander et al., 2019; Ulett et al., 2017). The use of advanced MRI methods such as diffusion or perfusion MRI has shown promise in the differentiation of gliomas from other types of lesions, but for infectious lesions including cryptococcomas, the limited data availability and relatively high variability has so far hindered conclusions about the added diagnostic value of these methods (Haris et al., 2008; Himmelreich and Gupta, 2006; Luthra et al., 2007; Nath et al., 2009). Moreover, common diagnostic tests for cryptococcosis such as culturing or antigen testing of cerebrospinal fluid (CSF) may be of limited value for cryptococcomas confined to the brain parenchyma (Mitchell et al., 1995; Singh et al., 2008). These diagnostic challenges hamper correct and rapid diagnosis and thereby delay the initiation of appropriate antifungal treatment or lead to unnecessary surgical procedures, which negatively impacts patients' outcome (Aye et al., 2016).

Previous studies have shown that MR spectroscopy allows *in vivo* detection of the fungal biomarker trehalose (Vanherp et al., 2021), a disaccharide that is produced in exceptionally high amounts by *Cryptococcus* spp. (Dzendrowskyj et al., 2005; Himmelreich et al., 2001; Petzold et al., 2006). Using a murine cryptococcoma model, we previously demonstrated that trehalose concentrations correlate to the viable fungal load, indicating that this quantitative biomarker holds high potential for both diagnostic and prognostic purposes (Vanherp et al., 2021). However, MRS has a poor spatial resolution and necessitates prior definition of relatively large voxels of interest for accurate detection, which leads to large partial volume effects in case of small lesions. Moreover, MRS can be challenging in case of lesions located close to the ventricles, sinuses or skull.

Chemical exchange saturation transfer (CEST) imaging is an advanced MRI technique that generates MR contrast based on the saturation of exchangeable protons in diverse molecules using selective radiofrequency pulses (Kogan et al., 2013; Van Zijl and Yadav, 2011; Ward et al., 2000). The saturated protons continuously exchange with the bulk water pool, and this saturation transfer results in a detectable decrease in the water signal and associated signal intensity in the MR image. By comparing the MRI contrast in CEST images acquired at different saturation offsets, the concentration of these exchangeable protons and compounds can indirectly be assessed with a relatively high spatial resolution and enhanced sensitivity. CEST contrast can be generated based on endogenous metabolites or after the administration of paramagnetic shift agents (Van Zijl and Yadav, 2011). CEST contrast based on endogenous metabolites has enabled successful imaging of various carbohydrates and polyols including glucose (Walker-Samuel et al., 2013), glycogen (van Zijl et al., 2007), myoinositol (Haris et al., 2011) and maltitol (Bagga et al., 2019), thanks to their exchanging hydroxyl protons. To date, the potential use of CEST imaging to assess endogenous metabolites of fungal cells in infectious lesions has not yet been explored. In this study, we investigated whether the potential CEST contrast generated by the high endogenous concentration of the disaccharide trehalose in cryptococcal cells enables *in vivo* detection of cryptococcomas in a murine model. Moreover, we tested whether the higher spatial resolution of CEST leads to an improved sensitivity for detecting small lesions compared to large lesions detected by MRS (Vanherp et al., 2021). We combined the information of various CEST offsets in the novel CryptoCEST contrast and assessed its potential for the spatially resolved identification of cryptococcomas and possible differentiation of cryptococcomas from gliomas.

2. Methods

2.1. Phantom experiments

D-(+)-trehalose dihydrate (Sigma-Aldrich, Saint Louis, MO, USA) and D-(+)-glucose (Fluka, Buchs, Switzerland) were dissolved in phosphate-buffered saline (PBS, Gibco, Paisley, USA). Solutions of 5, 10, 20, 30, 40 or 50 mM were transferred to 5 mm NMR tubes (Norell, Landisville, NJ, USA) for CEST imaging. All data represents average results from triplicate test tubes.

Wild-type *C. neoformans* H99 cells were plated on Sabouraud agar (Bio-Rad, Temse, Belgium) and incubated for 5 days at 30 °C. An inoculum was subsequently transferred to liquid Sabouraud medium and incubated for 24 h at 37 °C, while continuously shaking. Cultures were centrifuged and cells were washed twice with PBS. The number of cells was counted using a Neubauer counting chamber and diluted to 10^9 cells/ml in PBS. Serial dilutions were plated on Sabouraud agar and incubated for 4 days at room temperature to assess the number of colony-forming units (CFUs, corresponding to viable cells). Dilutions of different cell densities were transferred to 200 µl microcentrifuge tubes for imaging.

2.2. Animal experiments

All animal experiments were approved by the animal ethics committee of KU Leuven and conducted in accordance with European directive 2010/63/EU. Cryptococcal strains were cultured on Sabouraud agar and subsequently grown in liquid Sabouraud medium, both for 2–3 days at 30 °C. Inoculum preparation and cryptococcoma induction in mice were performed as previously described (Vanherp et al., 2020). In brief, cultures were centrifuged, washed twice with PBS, and the inoculum size was adjusted to the desired concentration after counting the cells with a Neubauer counting chamber. Unilateral focal brain lesions were induced by intracranial stereotactic injection of 10^4 *Cryptococcus* cells (1 µl) in the right striatum of female Balb/C mice (9–10 weeks old, Charles River or internal stock Animal Research Facility, KU Leuven). An additional control animal was injected with PBS. Orthotopic high-grade gliomas were generated by inoculating 5×10^3 neurospheres-cultured CT-2A cells in the brain of female C57BL/6 mice (12–14 weeks old, Envigo), as previously described (Riva et al., 2019). At the end of the experiment, mice were sacrificed using a pentobarbital overdose and the number of CFUs in the brain was determined as previously described (Vanherp et al., 2020).

2.2.1. Detection of small and larger cryptococcomas

Mice were injected intracranially with GFP-expressing *C. neoformans* H99 (n = 5) (Voelz et al., 2010) or PBS (n = 1) as control. MRS and CEST imaging was performed on day 3 and 6 post injection (p.i.).

2.2.2. Differentiation of cryptococcomas from gliomas

Mice were injected intracranially with *C. gattii* R265 (n = 6) or *C. neoformans* H99 (n = 5, both GFP-expressing (Voelz et al., 2010)), or neurospheres-cultured CT-2A cells (n = 3). To have a comparable lesion volume between the different models, MR spectra were acquired on day 10 (*C. neoformans*, separate set of animals), day 9 (*C. gattii*) or day 14 (gliomas) p.i., while CEST imaging was performed on day 8 (cryptococcomas) or day 14 (gliomas).

2.2.3. Treatment experiment

As previously described (Vanherp et al., 2020), mice (n = 16) were injected intracranially with bioluminescent *C. neoformans* KN99α (Vanherp et al., 2019) and received daily intraperitoneal injections with saline, liposomal amphotericin B (L-AMB, 10 mg/kg, AmbiSome, Gilead Sciences, Carrigtohill, Ireland) or fluconazole (75 mg/kg, TCI Europe, Zwijndrecht, Belgium) starting from day 3 p.i.. A fourth group received a single intravenous high dose of L-AMB (20 mg/kg) on day 3. CEST images were acquired on day 7 p.i. Other imaging read-outs of the same animals, including bioluminescence and MRS, were previously published in (Vanherp et al., 2020, 2021).

2.3. MR imaging

Images were acquired using a 9.4 T small animal horizontal MR system (BioSpec 94/20) with a linearly polarized resonator (all Bruker Biospin, Ettlingen, Germany) for transmission and an actively decoupled mouse brain surface coil for receiving. Animals were anesthetized using 1.5–2% isoflurane (Abbott Laboratories, Queensborough, UK) in 100% O_2. Breathing rate and body temperature of the animals were continuously monitored using a physiological monitoring system (Small Animal Instruments Inc., Stony Brook, NY, USA) and maintained around 80–120 breaths per minute and 37 ± 1 °C, respectively. For the phantoms, tubes were placed on top of an inverted mouse head coil because of rapid sedimentation of the cells in PBS.

2D axial T_2-weighted anatomical MRI scans were acquired using a fast spin-echo sequence (RARE) with repetition time (TR)/effective echo time (TE_{eff}) 4200/40 ms, RARE factor 8, matrix size 256 × 256, 9 contiguous slices of 0.5 mm thickness with 78 μm in-plane resolution (shown in the respective figures). To assist segmentation of the lesions for quantification of the CEST images, an additional axial scan with geometry identical to the CEST scans was acquired in case of smaller lesions (day 3 and 6), with a single slice of 1.5 mm thickness. Additional coronal scans were acquired as previously described (Vanherp et al., 2020) for positioning of the subsequent scans.

MR spectra were acquired from a 2 × 2 × 2 mm voxel placed inside or containing the brain lesion (depending on lesion volume), using a PRESS sequence with TR/TE 1800/20 ms, 320 averages, FASTMAP shimming (Gruetter, 1993), VAPOR water suppression and automatic acquisition of an unsuppressed reference scan (1 average) as described in (Vanherp et al., 2021).

Following a field map-based shim (MAPSHIM, Bruker BioSpin), CEST images were acquired using a RARE sequence with the following parameters: TR/TE 2620/23 ms, RARE factor 6, single slice of 1.5 mm thickness with matrix size 96 × 96 and 208 μm in-plane resolution. In all cases, a single axial slice was positioned over the center of the lesion. The saturation pulse train consisted of 300 × 8.5 ms pulses with a radiofrequency (RF) peak amplitude of 1.4 μT and a bandwidth of 150 Hz. In the full protocol, used for *in vitro* phantoms and the differentiation from gliomas, 107 CEST images were acquired at saturation frequency offsets (f_{sat}) ranging from −6.25 ppm to 6.25 ppm, as well as two control images at ±50 ppm. The f_{sat} intervals were 0.05 ppm if $|f_{sat}| \leq 0.3$ ppm, 0.1 ppm if $0.3 < |f_{sat}| \leq 4$ ppm and 0.25 ppm if $|f_{sat}| > 4$ ppm. This resulted in a total acquisition time of 45 min. For the phantom containing cryptococci, parameters were slightly adapted to a larger FOV with identical resolution and a TR/TE 2628/27.85 ms. For other studies (cryptococcomas of different sizes and antifungal treatment), a shorter protocol (30 min) was designed with only 71 CEST images, acquired at selected positive and negative saturation frequencies (in ppm): 20 offsets between 0 and 1 (0.05 step), 1.25, 1.875, 2.5, 6 offsets between 2.75 and 3.25 (0.1 step), 3.5, 3.75, 4.375, 5, 6.25 and 50 ppm.

2.4. Data analysis

MR spectra were manually phase-corrected and chemical shifts were referenced to residual water at 4.65 ppm using the TopSpin software (version 3.6.1, Bruker Biospin). Spectra were quantified using the AQSES algorithm (Poullet et al., 2007) in jMRUI (version 5.2, (Stefan et al., 2009)) to obtain absolute trehalose concentrations referenced to internal water (corrected for lesion volume), as described in (Vanherp et al., 2021).

CEST data processing was performed using custom-written Python scripts and ImageJ (Schneider et al., 2012) macros. Z-spectra, showing the ratio of MR signal intensity for a specific saturation offset and the 50 ppm reference offset, were corrected for B_0 inhomogeneity using the WASSR method with spline interpolation (bin size 0.1 ppm) (Kim et al., 2009). Magnetization transfer ratio asymmetry (MTR_{asym}) maps (in %) were generated according to the equation $MTR_{asym}(f) = 100 \times (S_{-f} - S_{+f})/S_{ref}$; where f is the frequency offset of interest, $S_{-f}$and S_{+f} are the corresponding signal intensities at the positive or negative saturation offset, and S_{ref} is the signal at the + 50 ppm offset. For presentation purposes, all maps were masked using a manually drawn brain mask.

CryptoCEST maps were generated in ImageJ using the following formula on every voxel of the brain masked images: $CryptoCEST\ contrast = |MTR_{asym}\ at\ 0.7\ ppm| / |MTR_{asym}\ at\ 4.0\ ppm|$. For figures, the CryptoCEST maps were smoothed using a 3 × 3 mean filter. Quantitative analysis was performed on log-transformed CryptoCEST data. Maps of the area under the curve (AUC) from 0.2 to 2 ppm were generated using a custom-written Python script.

The brain masks, regions of interest (ROI) in the cryptococcal lesions and contralateral reference ROIs were manually drawn on the T_2-weighted or CEST MR images using the adaptive brush tool in ITK-SNAP (Yushkevich et al., 2006). Reported lesion volumes represent the average volume of the coronal and axial T_2-weighted MRI scan. Reported CEST values represent mean signal intensities of the lesion ROI or contralateral ROI, for every replicate or animal, or as average for the group. To better assess potential intra-lesional differences, detailed quantitative analysis of treatment effects was performed using a histogram-based analysis of all voxels in the lesion ROI. The code and the datasets generated and analyzed during this study are available from the corresponding author on reasonable request.

2.5. Statistical analysis

Data was analyzed using GraphPad Prism (version 8.3.0, GraphPad Software Inc., San Diego, CA, USA). For the phantoms, the area under the curve between 0.2 and 2 ppm was calculated by including all peaks above baseline and simple linear regression (up to a concentration of 30 mM) was performed to assess concentration-dependencies. Correlation of the trehalose concentration and the CryptoCEST contrast was assessed using a Pearson correlation coefficient. CEST contrast between different lesions or treatment groups was compared using a one-way Welch's ANOVA test (assuming that groups have unequal variances) with Dunnett's T3 multiple comparisons test. Note that samples sizes for the glioma group (n = 3) were small. For the histogram-based analysis of treatment effects, the histogram (bin size 0.5 units) of the signal intensities of the voxels within the lesion ROI was normalized to the number of lesion voxels. This normalized histogram was averaged for the different animals within a group and a Gaussian curve was fitted to the average histogram using least squares fitting. In all cases, this resulted in an R^2 of at least 0.85.

3. Results

3.1. CEST imaging allows quantitative imaging of trehalose and Cryptococcus cells

To assess the feasibility and limit for detecting trehalose, we performed CEST imaging of *in vitro* phantoms containing different concentrations of glucose and trehalose in PBS. Both trehalose and glucose could be detected in concentrations as low as 5 mM in MTR_{asym} maps

acquired at 0.7 ppm (Fig. 1A). The shape of the Z-spectra and MTR_{asym} curves was highly comparable for both metabolites, with a strong CEST signal situated between 0.2 and 2 ppm and peaking around 0.7 ppm (Fig. 1B, C). For an identical molar concentration, the trehalose contrast was approximately twice the glucose contrast, as expected for the disaccharide. The area under the curve (0.2 – 2 ppm) was linearly dependent on the metabolite concentration up to 30 mM (Fig. 1D). At higher concentrations, the CEST contrast reached a saturation level. The ratio of the regression slopes for trehalose and glucose closely approximated their ratio of exchanging hydroxyl groups (8 and 5 groups, respectively). *Cryptococcus* cells showed a CEST contrast highly similar to trehalose, corresponding with their high intracellular trehalose concentration (Fig. 2). The contrast depended on the number of fungal cells. Reliable detection was possible from 2.53×10^7 viable cells (corresponding to 4×10^7 counted cells).

3.2. CryptoCEST contrast allows specific localization of cryptococcomas, even for small lesions

We subsequently investigated the detection and identification of cryptococcomas of various sizes using both CEST and MRS in a murine model. By day 6 p.i. of cryptococcal cells, all animals had developed a large, hyperintense brain lesion (Fig. 3A). CEST imaging allowed the discrimination of cryptococcomas from the surrounding brain tissue at offsets of 0.7 and 4 ppm. Cryptococcomas showed nearly symmetrical Z-spectra, but the contralateral brain tissue showed additional signals around +3.5, +2 and −4 ppm, likely corresponding to amide proton transfer (APT) (Zhou et al., 2003) and creatine/protein CEST effects (Cai et al., 2015; Zhang et al., 2017) and the aliphatic nuclear Overhauser (NOE) effect (Jin et al., 2013), respectively (Fig. 3B). Cryptococcomas had an MTR_{asym} pattern similar to the trehalose solutions and *Cryptococcus* phantoms, with a CEST signal between 0.2 and 2 ppm that reached its maximum around 0.7 ppm (Fig. 3C), while this signal was nearly absent in the contralateral brain tissue. At 4 ppm, we observed a strong negative contrast for the contralateral brain tissue, but not for cryptococcomas. The calculation of the ratio between the absolute values of the MTR_{asym} at 0.7 and 4 ppm enhanced the selective localization of cryptococcomas and discrimination from the normal brain tissue, and is therefore referred to as the CryptoCEST contrast (Fig. 3A). Proton MRS of a voxel placed inside the cryptococcoma confirmed the presence of trehalose as the main metabolite, with a strong isolated signal of the anomeric hydrogen at 5.2 ppm and resonances of the other hydrogens around 3.4–3.8 ppm. (Fig. 3D). In general, a higher fungal burden (CFU) in the brain corresponded to a larger lesion area with higher trehalose concentrations and higher CryptoCEST signal intensity (Supplementary Table 1).

At an earlier timepoint (day 3 p.i.), CEST imaging allowed detection of some cryptococcomas even smaller than 1 mm^3, in particular in the CryptoCEST contrast map (Fig. 4A). We observed some aspecific CryptoCEST contrast near the edges of the brain and the inferior venous sinus, but comparison to the T_2-weighted MRI scans allowed distinction from actual lesions. MTR_{asym} spectra corresponded to those observed for larger cryptococcomas, but with a lower contrast intensity (Fig. 4B). Although a large inter-animal variability was observed, the quantified CryptoCEST contrast was higher in all cryptococcomas than in the contralateral brain tissue (Fig. 4C). No CryptoCEST contrast was observed in a control animal injected with PBS (Fig. S1). Unlike the CryptoCEST results, localized MR spectra of the small lesions (<1 mm^3) were poorly distinguishable from the normal brain and showed limited trehalose resonances (Fig. 4D). Quantification of MR spectra indicated trehalose concentrations below 5 mM (Supplementary Table 2). The CryptoCEST contrast in the small and larger cryptococcal lesions correlated well with the quantified trehalose concentration in the MRS voxel (Fig. S2).

3.3. CryptoCEST can differentiate between cryptococcomas and gliomas

We tested the added value of CEST imaging for differentiating

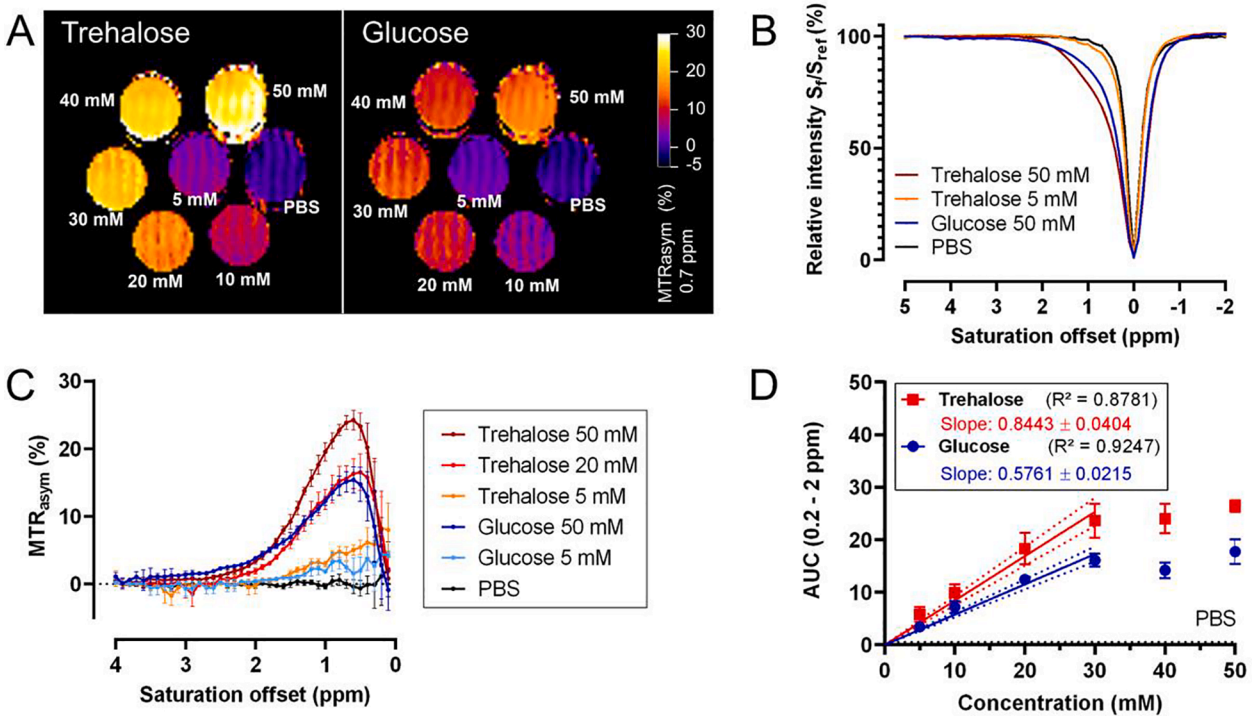

Fig. 1. Concentration-dependent CEST contrast of glucose and trehalose solutions. A) MTR_{asym} maps at 0.7 ppm. B-C) Z-spectrum (B) and MTR_{asym} curves (C) of selected glucose and trehalose concentrations in PBS. D) Linear regression of the area under the curve (AUC) from 0.2 to 2 ppm and the glucose or trehalose concentration (up to 30 mM), with estimated slope ± SE. At higher concentrations, the AUC approached saturation. The dotted black line represents the mean for the PBS samples. All graphs show mean (±SD) of triplicate test tubes.

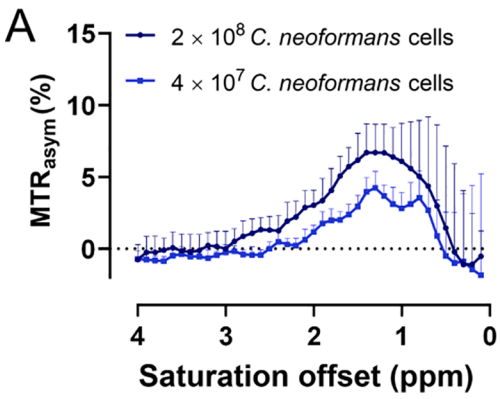

B

Cells / sample	CFUs / sample	AUC (0.2 – 2 ppm)
2×10^8	1.27×10^8	7.766
4×10^7	2.53×10^7	3.949
8×10^6	5.06×10^6	Not detectable

Fig. 2. CEST imaging of *Cryptococcus* cell phantoms. *C. neoformans* cells were suspended in PBS, counted and afterwards plated for colony-forming unit (CFU) counting. A) MTR_{asym} curves and B) quantification of the area under the curve (AUC, from 0.2 to 2 ppm) for different cell densities.

between cryptococcomas caused by *C. neoformans* or *C. gattii* and gliomas. Both types of cryptococcomas and gliomas were visible as hyperintense lesions on the T_2-weighted MRI (Fig. 5A). MRS confirmed the presence of trehalose in cerebral cryptococcomas, while gliomas were characterized by an increased choline/creatine ratio and the presence of lipids (Figure S3).

Z-spectra and MTR_{asym} curves showed distinct patterns for the different lesion types (Fig. 5 B, C). Both types of cryptococcomas showed nearly symmetrical Z-spectra, but these were narrower for *C. gattii* lesions than *C. neoformans* lesions. Similar to the normal brain tissue, gliomas displayed additional CEST or NOE signals around +3.5, +2 and −4 ppm, while these signals were absent in the cryptococcomas. CEST imaging allowed identification and localization of cryptococcomas based on the MTR_{asym} maps at 0.7 ppm, while gliomas were not visible at this offset (Fig. 5A, D). At 4 ppm, cryptococcomas could also be distinguished from the surrounding brain, while gliomas were also discernible on the 4 ppm image but did not have a significantly higher MTR_{asym} compared to the contralateral brain (Fig. 5 A, E). Calculation of the CryptoCEST contrast allowed clear distinction between cryptococcomas and gliomas or the contralateral brain tissue (Fig. 5 A, F).

3.4. Suboptimal antifungal treatment only induces minor changes in the CryptoCEST contrast

Finally, we assessed the effect of antifungal treatment with liposomal amphotericin B and fluconazole on the CryptoCEST contrast. At day 7 p.i., 3 days after initiation of antifungal treatment, CEST images and MTR_{asym} curves of the treated and untreated groups were comparable (Fig. 6). Quantification of the MTR_{asym} signal at 0.7 ppm, the AUC (0.2 – 2 ppm) and the CryptoCEST contrast showed a slight trend towards lower signal intensities in the groups treated with liposomal amphotericin B (Fig. S4). These only minor changes are congruent with the limited efficacy of these treatment regimens as analysis of the fungal burden at day 9 p.i. only showed a 10-fold reduction in CFUs following fluconazole treatment and 4-fold reduction in 3 out of 4 animals receiving liposomal amphotericin B daily, as previously described (Vanherp et al., 2020, 2021) (Fig. S5).

4. Discussion

In this study, we investigated the potential of CEST-based MR imaging of cryptococcal brain infections in a murine model. Thanks to the high endogenous concentration of the fungal biomarker trehalose in cryptococcomas, the CryptoCEST contrast allowed detection and specific spatial localization of cryptococcomas, even for relatively small fungal lesions. Moreover, it enabled indirect quantitative analysis of the endogenous trehalose concentrations and non-invasive differentiation of cryptococcomas from gliomas.

In vitro, the fungal biomarker trehalose generated a broad concentration-dependent CEST contrast between 0.2 and 2 ppm, with a maximum around 0.7 ppm. This corresponds to the typical offset range for exchanging hydroxyl groups (Kogan et al., 2013), as seen for other sugars and polyols like glucose (Walker-Samuel et al., 2013), glycogen (van Zijl et al., 2007), myoinositol (Haris et al., 2011) and maltitol (Bagga et al., 2019). While the MTR_{asym} curve was comparable for trehalose and glucose, the CEST contrast for trehalose was approximately twice as high due to nearly twice the number of exchanging groups. *In vitro*, we were able to reliably detect as little as 2.5×10^7 cryptococcal cells, but rapid sedimentation of the cells hampered an accurate assessment of the sensitivity. *In vivo* applications showed that lesions of 7.6×10^5 CFUs and even smaller were easily detectable due to the high localized fungal cell density and high trehalose concentration produced by cryptococci in the host environment (Vanherp et al., 2021).

As the endogenous trehalose concentrations in cryptococcomas (typically between 5 and 30 mM, (Vanherp et al., 2021)) exceed those for glucose and myoinositol in the mouse or human brain (typically between 1 and 5 mM (Khlebnikov et al., 2019; Tkáč et al., 2004)), the CEST contrast allowed discrimination of cryptococcomas from the normal brain tissue at 0.7 ppm. Although this offset is likely the most selective biomarker for trehalose and thus cryptococcomas, the close proximity of this offset to 0 typically leads to a lower signal-to-noise ratio (SNR). Therefore, we also investigated additional offsets. At 4 ppm, we observed a strong negative contrast for the normal brain, likely due to a combination of APT CEST (+3.5 ppm) and aliphatic NOE effects (-4 ppm) originating from various brain metabolites (Khlebnikov et al., 2019). The observed inter-animal variability at this offset is difficult to attribute to a specific metabolite as the APT and NOE signals cannot be discriminated in the MTR_{asym} analysis, but alterations in the NOE effect have previously also been described in the contralateral hemisphere of an ischemic stroke model (Li et al., 2015). The contrasting loss of the APT CEST and NOE signals in the cryptococcomas is likely due to the absence or low amount of mammalian cells in these regions, and could be seen as a potential additional biomarker suggestive for a space-occupying lesion consisting of microbial cells.

By combining the selectivity of 0.7 ppm with the higher SNR of the 4 ppm offset in the CryptoCEST contrast, we were able to enhance the spatial localization of cryptococcomas. The CryptoCEST contrast in a lesion correlated well with the trehalose concentration in that region, indicating that the contrast can largely be attributed to this most abundant fungal metabolite. An inherent limitation of CEST imaging is the lack of specificity to discriminate between chemically similar hydroxyl groups, so other fungal carbohydrates or polyols can possibly also further contribute to the signal. Notably, we have previously shown higher trehalose concentrations in cryptococcomas caused by *C. neoformans* than in those caused by *C. gattii*, but observed a stronger CryptoCEST contrast for the latter. Whether this is caused by the

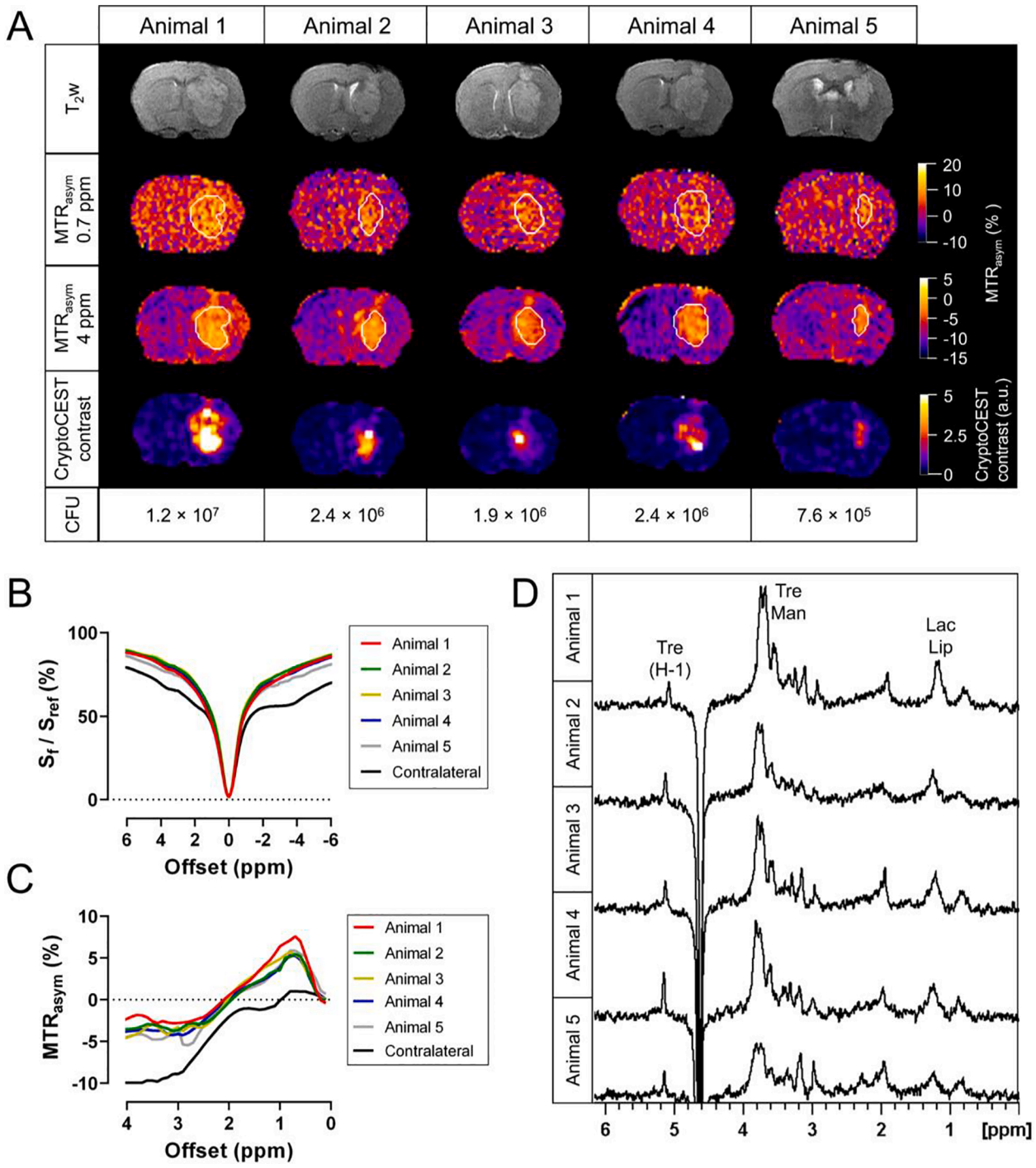

Fig. 3. Detection of large cryptococcomas using T_2-weighted MR imaging, CEST imaging and localized MRS. Mice (n = 5) were stereotactically injected in the brain with *C. neoformans* (H99) to induce localized cryptococcomas. Mouse brains were imaged on day 6 p.i. A) T_2-weighted axial MRI scans, MTR_{asym} maps at 0.7 and 4 ppm, CryptoCEST contrast maps, and the number of colony-forming units (CFU) in the brain for the different animals. The borders of the lesion are indicated with a white line on the MTR_{asym} maps. The single imaging slice was positioned over the center of the lesion. B-C) Z-spectra (B) and MTR_{asym} (C) curves of the cryptococcoma (per animal) and contralateral normal brain region (averaged for different animals). D) Localized ^{1}H-MR spectra acquired from a 2 × 2 × 2 mm voxel placed inside the cryptococcoma. Abbreviations: Tre: trehalose; H-1: resonance of the anomeric hydrogen of trehalose; Man: mannitol; Lip: lipids; Lac: lactate.

presence of other carbohydrates/polyols such as mannitol, or is mediated by differences in the lesion composition, water content, T_2-relaxation rate or pH requires more investigation.

The CryptoCEST contrast permitted us to identify and localize cryptococcomas even smaller than 1 mm^3. With MRS, trehalose was poorly detectable in these small lesions because of the partial volume effect in the large voxels required for MRS, which diluted the signal. As such, CEST imaging offers a greater sensitivity for trehalose-based *in vivo* identification of cryptococcomas when compared to MRS and also provides a precise spatial localization of cryptococcal lesions. So far, detection was not feasible for all small lesions tested due to partial volume effects associated with the relatively large slice thickness used in our CEST imaging protocol. Moreover, B1 inhomogeneity was not corrected in our study and may lead to small artefacts at high field strengths. Further technological improvements such as B1 inhomogeneity corrections (Sun et al., 2007; Windschuh et al., 2015),

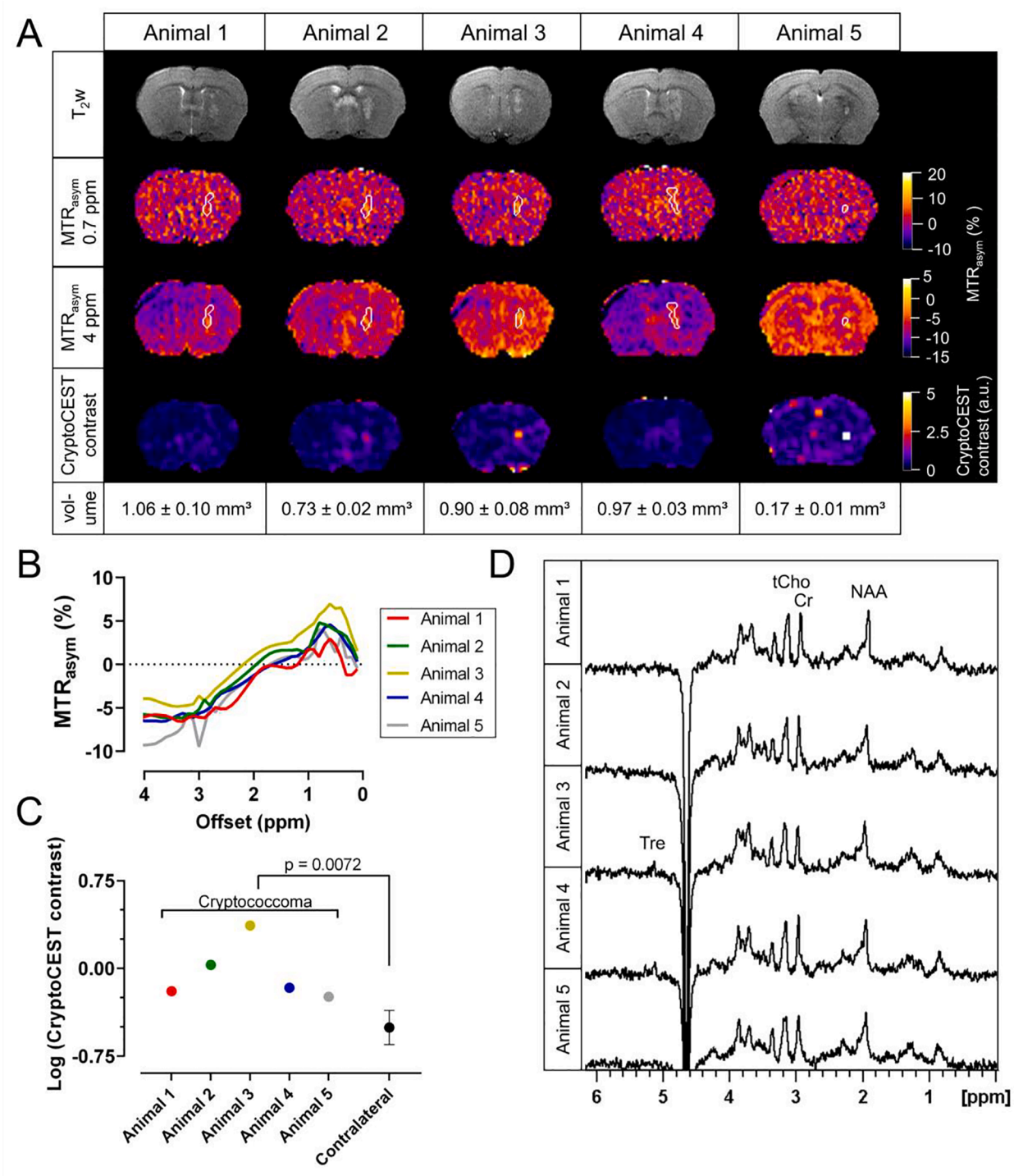

Fig. 4. Localization of small cryptococcomas using CryptoCEST imaging. Mice were imaged 3 days after intracranial injection of *C. neoformans* (H99) cells. A) T_2-weighted axial MRI scans, MTR_{asym} maps at 0.7 and 4 ppm, CryptoCEST contrast maps, and the lesion volume of the cryptococcoma for the different animals as determined from the T_2-weighted MRI. The single CEST imaging slice was positioned over the center of the lesion. B) MTR_{asym} curves of the cryptococcomas. C) Quantification of the average log-transformed CryptoCEST contrast in the lesions of individual mice and the contralateral ROI (averaged for different animals). The log (CryptoCEST contrast) was significantly higher in the cryptococcomas than the contralateral brain tissue (unpaired *t*-test of grouped data). D) Localized MR spectra acquired with the volume of interest (2 × 2 × 2 mm) placed around the lesion. Abbreviations: tCho: total choline; Cr: creatine; NAA: N-acetylaspartate; Tre: trehalose.

thinner acquisition slices or improved quantification strategies for resolving individual contributions of different effects to the Z-spectrum (Desmond et al., 2014; Zhou et al., 2017) could potentially enhance the detection of these small lesions.

While cryptococcomas and gliomas appear very similar on conventional T_2-weighted MRI, CEST imaging enabled differentiation of both lesion types, depending on the chosen offset. Gliomas were characterized by a mostly absent CEST contrast at 0.7 ppm due to low endogenous concentrations of carbohydrates or polyols (Bagga et al., 2019). At around 4 ppm previously described differences in APT CEST and NOE contributions provided a moderately higher CEST contrast for gliomas than the normal brain (Roussel et al., 2018; Xu et al., 2014). Although

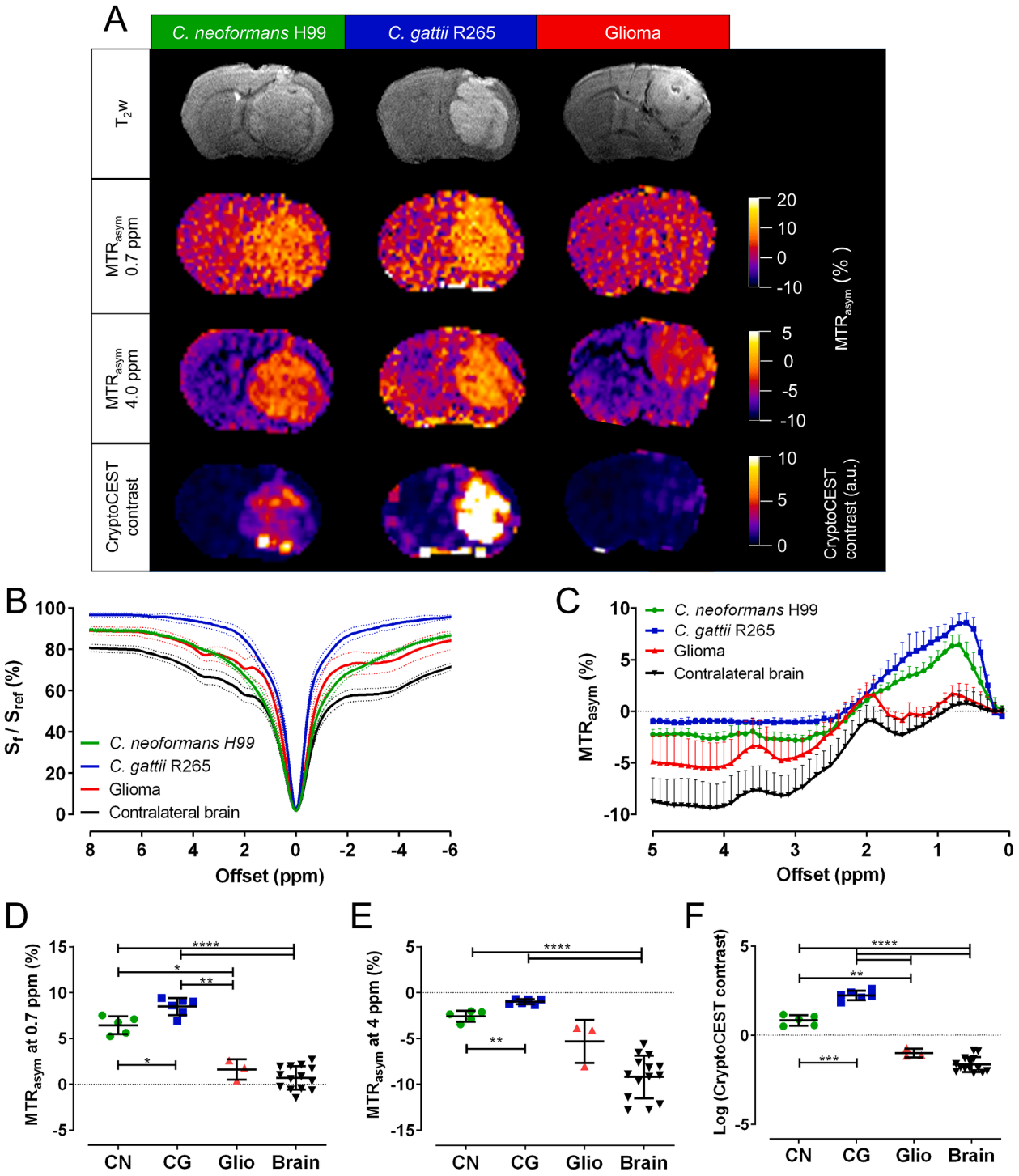

Fig. 5. CEST imaging of mice with cryptococcomas and gliomas. Mice were injected intracranially with *C. neoformans* (H99) cells (n = 5), *C. gattii* (R265) cells (n = 6) or neurospheres-cultured CT-2A cells (n = 3). CEST images were acquired 8 days (cryptococcoma) or 14 days after inoculation (glioma). A) T_2-weighted anatomical MRIs, MTR_{asym} maps at 0.7 and 4 ppm, and CryptoCEST maps for representative animals. B) Z-spectra. C) MTR_{asym} curves. D-F) Quantification of the MTR_{asym} contrast at 0.7 ppm (D), at 4 ppm (E) and logarithm of the CryptoCEST contrast (F) for *C. neoformans* (CN) and *C. gattii* (CG) cryptococcomas, gliomas (Glio) and the contralateral brain tissue (Brain). All graphs show individual values and/or mean + or ± SD per group, Welch's ANOVA with Dunnett's T3 post-test. *: $p < 0.05$, **: $p < 0.01$; ***: $p < 0.001$; ****: $p < 0.0001$.

there may be small variations in CEST contrast with tumor progression and between different glioma models (Cai et al., 2017), combining this information in the CryptoCEST contrast enabled selective visualization of cryptococcomas compared to the tested gliomas and the normal brain tissue. Our study suggests that upon translation to the clinic, CryptoCEST could be used to differentiate cryptococcomas from gliomas and thereby prevent a common initial misdiagnosis and unnecessary surgery, leading to more rapid initiation of appropriate antifungal therapy.

Aside from cryptococcosis, various other types of infections may cause brain lesions and require differential diagnosis, but to date, only few applications of CEST MRI for infectious diseases have been described. In a recent clinical study, both infective and neoplastic mass

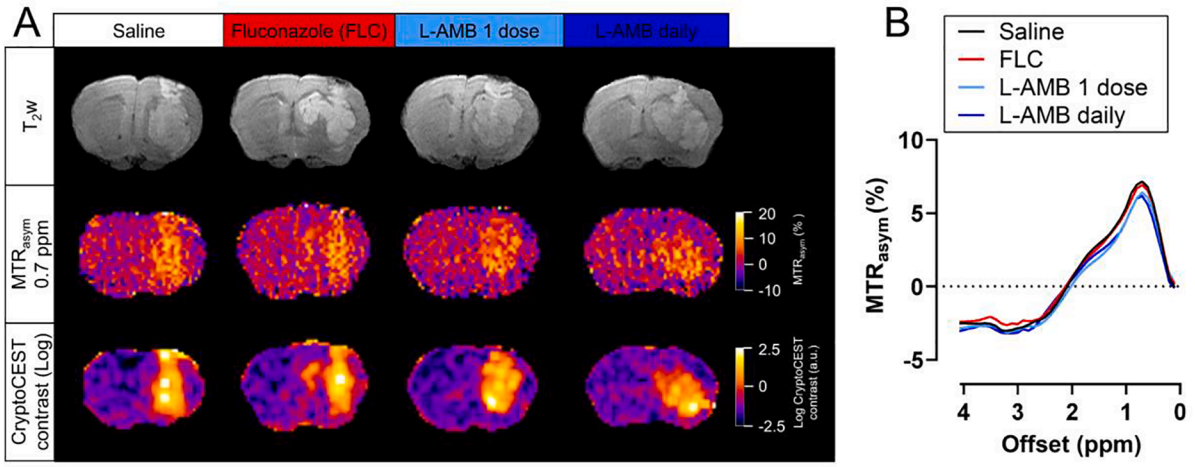

Fig. 6. CEST imaging of cryptococcomas after antifungal treatment. Starting from day 3 p.i., animals (n = 4 per group) received daily intraperitoneal injections of saline, fluconazole (FLC) or liposomal amphotericin B (L-AMB), or a single high intravenous dose of L-AMB. A) T_2-weighted axial MRI scans, MTR_{asym} maps at 0.7 ppm and (log) CryptoCEST maps for representative animals. B) MTR_{asym} curves, averaged for animals within a respective group.

lesions showed a higher APT-CEST contrast than the contralateral side of the brain (Debnath et al., 2020). AcidoCEST-based quantification of the tissue pH enabled indirect detection of the pulmonary fungal infection coccidioidomycosis and allowed differentiation from lung cancer in mice (Lindeman et al., 2019). An enhanced glutamate CEST (GluCEST) signal was noted in both rat models and human patients with *Staphylococcus aureus* encephalitis, possibly caused by the inflammatory response (Chen et al., 2018; Jia et al., 2020). Other preclinical studies with *S. aureus* abscesses or tumor-homing *Clostridium novyi-NT* bacteria reported a broad CEST signal in the 0.5 – 4 ppm range with a maximum around 2.6 ppm, likely originating from various endogenous bacterial macro-metabolites (bacCEST) (Liu et al., 2013, 2018). In our application, the origin of the CryptoCEST contrast was directly attributed to the high endogenous concentration of trehalose in cryptococcal cells and was mainly situated between 0.2 and 2 ppm. For validation that these differences are large enough to also enable differentiation of cryptococcomas and bacterial abscesses, further investigation using the same B_1 field strength would be required. Furthermore, the potential CEST contrast generated by other fungal infections remains to be explored. Although *Cryptococcus* typically produces trehalose at much higher concentrations than other organisms (Himmelreich et al., 2001), recent studies have described a pan-fungal disaccharide marker in serum of infected patients (Cornu et al., 2019), possibly trehalose. If this marker or other carbohydrates reach localized high concentrations in other types of fungal lesions, this could potentially lead to a similar CEST contrast. Investigation of the CEST contrast in other infectious lesions would be needed to determine the ultimate specificity of the CryptoCEST contrast for etiological diagnosis.

In our studies, we only observed a very small change in the CryptoCEST contrast upon antifungal treatment due to low treatment efficacy. In comparison to bacterial infections, fungal infections typically require prolonged treatment and are generally difficult to treat due to issues regarding drug bio-availability and toxicity, which was confirmed in our study. In the same group of animals, we previously showed that systemic treatment with a single antifungal has a limited efficacy for several reasons and could slow down but not halt or reverse the growth of the cryptococcoma, restricting the survival period and possibilities for prolonged treatment in mice (Vanherp et al., 2020). MRS previously showed a lower trehalose concentration in cryptococcomas of mice treated with fluconazole or treated intralesionally with L-AMB compared to untreated mice (Vanherp et al., 2021). Yet, concentrations obtained by quantification of MRS data can also be influenced by the size of the lesion and the associated partial volume effect. In CEST MRI, a therapy-induced decrease in the trehalose concentration may also be obscured by the presence of other intermediates in the catabolism of trehalose, which we previously investigated in *C. neoformans* cultures (Vanherp et al., 2021). Further studies using more efficacious treatment regimens such as combination therapy (Brouwer et al., 2004; Santos et al., 2017) will be required to assess the full potential of applying CEST imaging to follow-up antifungal treatment efficacy.

In conclusion, our results showed that CryptoCEST enables the identification, spatial localization and differentiation of cryptococcal lesions from brain tumors. Moreover, CryptoCEST had a higher sensitivity for trehalose-based detection of small cryptococcomas compared to MRS, due to partial volume effects associated with the latter. Molecular imaging based on CEST has been actively explored for various clinical applications, but to date mainly in a research setting. Several previous studies have already shown that translation of preclinical CEST results to applications at clinical field strengths is feasible, although challenging for carbohydrate CEST imaging (Kim et al., 2019; Wang et al., 2016; Xu et al., 2020). With recent developments in more rapid acquisition methods (possibly including a selection of specific offsets), hardware improvements, and standardization of acquisition and processing methodology, routine clinical use comes within reach (Jones et al., 2018; Zhou et al., 2019). Thanks to the high endogenous concentration of trehalose in cryptococcomas, CryptoCEST does not require exogeneous administration of a contrast agent, which makes the technique easy to implement. Translation to clinical practice holds high potential for non-invasive differential diagnosis of cryptococcomas from other types of brain pathologies, in particular brain tumors, which would reduce the time needed to start appropriate treatment and thereby improve patients' outcomes.

CRediT authorship contribution statement

Liesbeth Vanherp: Conceptualization, Formal analysis, Investigation, Methodology, Validation, Visualization, Data curation, Writing - original draft. **Kristof Govaerts:** Conceptualization, Formal analysis, Investigation, Methodology, Software, Validation, Data curation, Writing - review & editing. **Matteo Riva:** Resources, Writing - review & editing. **Jennifer Poelmans:** Investigation. **An Coosemans:** Resources, Writing - review & editing. **Katrien Lagrou:** Resources, Writing - review & editing. **Willy Gsell:** Methodology, Validation, Writing - review & editing. **Greetje Vande Velde:** Resources, Writing - review & editing, Supervision, Funding acquisition. **Uwe Himmelreich:** Conceptualization, Resources, Writing - review & editing, Supervision, Project

administration, Funding acquisition.

Declaration of Competing Interest

The authors declare that they have no known competing financial interests or personal relationships that could have appeared to influence the work reported in this paper.

Acknowledgements

The authors would like to thank Jens Wouters and dr. Sarah Belderbos for their technical assistance. We are grateful to Dr. Didier Wecker and Bruker BioSpin for providing the CEST MR module. This work was supported by the European ERA-NET project 'CryptoView' (3rd call of the FP7 program Infect-ERA), the European H2020-MSCA-ITN 'INSPiRE-MED' (813120), the Research Foundation-Flanders (FWO, 1506114N, 151313 to LV and 12N7615N to GVV), the Agency for Innovation by Science and Technology (IWT, 141230 to JP) and KU Leuven (PF 10/017 (IMIR), CREA/14/015 to GVV).

Appendix A. Supplementary data

Supplementary data to this article can be found online at https://doi.org/10.1016/j.nicl.2021.102737.

References

Aye, C., Henderson, A., Yu, H., Norton, R., 2016. Cryptococcosis—the impact of delay to diagnosis. Clin. Microbiol. Infect. 22 (7), 632–635. https://doi.org/10.1016/j.cmi.2016.04.022.

Bagga, P., Wilson, N., Rich, L., Marincola, F.M., Schnall, M.D., Hariharan, H., Haris, M., Reddy, R., 2019. Sugar alcohol provides imaging contrast in cancer detection. Sci. Rep. 9, 11092. https://doi.org/10.1038/s41598-019-47275-5.

Beardsley, J., Sorrell, T.C., Chen, S.C.A., 2019. Central nervous system cryptococcal infections in non-HIV infected patients. J. Fungi 5, 71. https://doi.org/10.3390/jof5030071.

Brouwer, A.E., Rajanuwong, A., Chierakul, W., Griffin, G.E., Larsen, R.A., White, N.J., Harrison, T.S., 2004. Combination antifungal therapies for HIV-associated cryptococcal meningitis: a randomised trial. Lancet 363 (9423), 1764–1767. https://doi.org/10.1016/S0140-6736(04)16301-0.

Cai, K., Singh, A., Poptani, H., Li, W., Yang, S., Lu, Y., Hariharan, H., Zhou, X.J., Reddy, R., 2015. CEST signal at 2 ppm (CEST at 2ppm) from Z-spectral fitting correlates with creatine distribution in brain tumor. NMR Biomed. 28, 1–8. https://doi.org/10.1002/nbm.3216.

Cai, K., Tain, R.-W., Zhou, X.J., Damen, F.C., Scotti, A.M., Hariharan, H., Poptani, H., Reddy, R., 2017. Creatine CEST MRI for differentiating gliomas with different degrees of aggressiveness. Mol. Imaging Biol. 19 (2), 225–232. https://doi.org/10.1007/s11307-016-0995-0.

Charlier, C., Dromer, F., Lévêque, C., Chartier, L., Cordoliani, Y.-S., Fontanet, A., Launay, O., Lortholary, O., Mylonakis, E., 2008. Cryptococcal neuroradiological lesions correlate with severity during cryptococcal meningoencephalitis in HIV-positive patients in the HAART Era. PLoS One 3 (4), e1950. https://doi.org/10.1371/journal.pone.0001950.

Chen, Y., Dai, Z., Shen, Z., Guan, J., Zhuang, Z., Mao, Y., Wu, R., 2018. Imaging of glutamate in brain abscess using GLUCEST at 7T. Radiol. Infect. Dis. 5 (4), 148–153. https://doi.org/10.1016/j.jrid.2018.11.001.

Chen, S., Sorrell, T., Nimmo, G., Speed, B., Currie, B., Ellis, D., Marriott, D., Pfeiffer, T., Parr, D., Byth, K., 2000. Epidemiology and Host- and Variety-Dependent Characteristics of Infection Due to *Cryptococcus neoformans* in Australia and New Zealand. Clin. Infect. Dis. 31, 499–508. https://doi.org/10.1086/313992.

Cornu, M., Sendid, B., Mery, A., François, N., Mikulska, M., Letscher-Bru, V., De Carolis, E., Damonti, L., Titecat, M., Bochud, P.-Y., Alanio, A., Sanguinetti, M., Viscoli, C., Herbrecht, R., Guerardel, Y., Poulain, D., Warnock, D.W., 2019. Evaluation of mass spectrometry-based detection of panfungal serum disaccharide for diagnosis of invasive fungal infections: results from a collaborative study involving Six European clinical centers. J. Clin. Microbiol. 57 (5) https://doi.org/10.1128/JCM.01867-18.

Debnath, A., Gupta, R.K., Singh, A., 2020. Evaluating the Role of Amide Proton Transfer (APT)–Weighted Contrast, Optimized for Normalization and Region of Interest Selection, in Differentiation of Neoplastic and Infective Mass Lesions on 3T MRI. Mol. Imaging Biol. 22 (2), 384–396. https://doi.org/10.1007/s11307-019-01382-x.

Desmond, K.L., Moosvi, F., Stanisz, G.J., 2014. Mapping of amide, amine, and aliphatic peaks in the CEST spectra of murine xenografts at 7 T. Magn. Reson. Med. 71 (5), 1841–1853. https://doi.org/10.1002/mrm.24822.

Dzendrowskyj, T.E., Dolenko, B., Sorrell, T.C., Somorjai, R.L., Malik, R., Mountford, C.E., Himmelreich, U., 2005. Diagnosis of cerebral cryptococcoma using a computerized analysis of 1H NMR spectra in an animal model. Diagn. Microbiol. Infect. Dis. 52 (2), 101–105. https://doi.org/10.1016/j.diagmicrobio.2005.02.004.

Gruetter, R., 1993. Automatic, localized *in Vivo* adjustment of all first-and second-order shim coils. Magn. Reson. Med. 29 (6), 804–811. https://doi.org/10.1002/mrm.1910290613.

Haris, M., Gupta, R.K., Singh, A., Husain, N., Husain, M., Pandey, C.M., Srivastava, C., Behari, S., Rathore, R.K.S., 2008. Differentiation of infective from neoplastic brain lesions by dynamic contrast-enhanced MRI. Neuroradiology 50 (6), 531–540. https://doi.org/10.1007/s00234-008-0378-6.

Haris, M., Cai, K., Singh, A., Hariharan, H., Reddy, R., 2011. *In vivo* mapping of brain myo-inositol. Neuroimage 54 (3), 2079–2085. https://doi.org/10.1016/j.neuroimage.2010.10.017.

Himmelreich, U., Gupta, R.K., 2006. Application of Magnetic Resonance for the Diagnosis of Infective Brain Lesions, Modern Magnetic Resonance. Springer Netherlands, Dordrecht. DOI:10.1007/1-4020-3910-7.

Himmelreich, U., Dzendrowskyj, T.E., Allen, C., Dowd, S., Malik, R., Shehan, B.P., Russell, P., Mountford, C.E., Sorrell, T.C., 2001. Cryptococcomas distinguished from gliomas with MR spectroscopy: an experimental rat and cell culture study. Radiology 220 (1), 122–128. https://doi.org/10.1148/radiology.220.1.r01jl25122.

Jia, Y., Chen, Y., Geng, K., Cheng, Y., Li, Y., Qiu, J., Huang, H., Wang, R., Zhang, Y., Wu, R., 2020. Glutamate Chemical Exchange Saturation Transfer (GluCEST) magnetic resonance imaging in pre-clinical and clinical applications for encephalitis. Front. Neurosci. 14 https://doi.org/10.3389/fnins.2020.00750.

Jin, T., Wang, P., Zong, X., Kim, S.-G., 2013. MR imaging of the amide-proton transfer effect and the pH-insensitive nuclear overhauser effect at 9.4 T. Magn. Reson. Med. 69 (3), 760–770. https://doi.org/10.1002/mrm.24315.

Jones, K.M., Pollard, A.C., Pagel, M.D., 2018. Clinical applications of chemical exchange saturation transfer (CEST) MRI. J. Magn. Reson. Imaging 47 (1), 11–27. https://doi.org/10.1002/jmri.25838.

Khlebnikov, V., van der Kemp, W.J.M., Hoogduin, H., Klomp, D.W.J., Prompers, J.J., 2019. Analysis of chemical exchange saturation transfer contributions from brain metabolites to the Z-spectra at various field strengths and pH. Sci. Rep. 9, 1–11. https://doi.org/10.1038/s41598-018-37295-y.

Kim, M., Gillen, J., Landman, B.A., Zhou, J., van Zijl, P.C.M., 2009. Water saturation shift referencing (WASSR) for chemical exchange saturation transfer (CEST) experiments. Magn. Reson. Med. 61 (6), 1441–1450. https://doi.org/10.1002/mrm.21873.

Kim, M., Torrealdea, F., Adeleke, S., Rega, M., Evans, V., Beeston, T., Soteriou, K., Thust, S., Kujawa, A., Okuchi, S., Isaac, E., Piga, W., Lambert, J.R., Afaq, A., Demetriou, E., Choudhary, P., Cheung, K.K., Naik, S., Atkinson, D., Punwani, S., Golay, X., 2019. Challenges in glucoCEST MR body imaging at 3 Tesla. Quant. Imaging Med. Surg. 9, 1628–1640. https://doi.org/10.21037/qims.2019.10.05.

Kogan, F., Hariharan, H., Reddy, R., 2013. Chemical Exchange Saturation Transfer (CEST) imaging: description of technique and potential clinical applications. Curr. Radiol. Rep. 1 (2), 102–114. https://doi.org/10.1007/s40134-013-0010-3.

Li, Q., You, C., Liu, Q., Liu, Y., 2010. Central nervous system cryptococcoma in immunocompetent patients: a short review illustrated by a new case. Acta Neurochir. (Wien) 152 (1), 129–136. https://doi.org/10.1007/s00701-009-0311-8.

Li, H., Zu, Z., Zaiss, M., Khan, I.S., Singer, R.J., Gochberg, D.F., Bachert, P., Gore, J.C., Xu, J., 2015. Imaging of amide proton transfer and nuclear Overhauser enhancement in ischemic stroke with corrections for competing effects. NMR Biomed. 28 (2), 200–209. https://doi.org/10.1002/nbm.3243.

Lindeman, L.R., Jones, K.M., High, R.A., Howison, C.M., Shubitz, L.F., Pagel, M.D., 2019. Differentiating lung cancer and infection based on measurements of extracellular pH with acidoCEST MRI. Sci. Rep. 9, 1–8. https://doi.org/10.1038/s41598-019-49514-1.

Liu, J., Bai, R., Li, Y., Staedtke, V., Zhang, S., van Zijl, P.C.M., Liu, G., 2018. MRI detection of bacterial brain abscesses and monitoring of antibiotic treatment using bacCEST. Magn. Reson. Med. 80 (2), 662–671. https://doi.org/10.1002/mrm.27180.

Liu, G., Bettegowda, C., Qiao, Y., Staedtke, V., Chan, K.W.Y., Bai, R., Li, Y., Riggins, G.J., Kinzler, K.W., Bulte, J.W.M., McMahon, M.T., Gilad, A.A., Vogelstein, B., Zhou, S., van Zijl, P.C.M., 2013. Noninvasive imaging of infection after treatment with tumor-homing bacteria using Chemical Exchange Saturation Transfer (CEST) MRI. Magn. Reson. Med. 70 (6), 1690–1698. https://doi.org/10.1002/mrm.24955.

Luthra, G., Parihar, A., Nath, K., Jaiswal, S., Prasad, K.N., Husain, N., Husain, M., Singh, S., Behari, S., Gupta, R.K., 2007. Comparative evaluation of fungal, tubercular, and pyogenic brain abscesses with conventional and diffusion MR imaging and proton MR spectroscopy. AJNR. Am. J. Neuroradiol. 28 (7), 1332–1338. https://doi.org/10.3174/ajnr.A0548.

Maziarz, E.K., Perfect, J.R., 2016. Cryptococcosis. Infect. Dis. Clin. North Am. 30 (1), 179–206. https://doi.org/10.1016/j.idc.2015.10.006.

Mitchell, D.H., Sorrell, T.C., Allworth, A.M., Heath, C.H., McGregor, A.R., Papanaoum, K., Richards, M.J., Gottlieb, T., 1995. Cryptococcal disease of the CNS in immunocompetent hosts: influence of cryptococcal variety on clinical manifestations and outcome. Clin. Infect. Dis. 20 (3), 611–616. https://doi.org/10.1093/clinids/20.3.611.

Nath, K., Agarwal, M., Ramola, M., Husain, M., Prasad, K.N., Rathore, R.K.S., Pandey, C. M., Gupta, R.K., 2009. Role of diffusion tensor imaging metrics and in vivo proton magnetic resonance spectroscopy in the differential diagnosis of cystic intracranial mass lesions. Magn. Reson. Imaging 27 (2), 198–206. https://doi.org/10.1016/j.mri.2008.06.006.

Petzold, E.W., Himmelreich, U., Mylonakis, E., Rude, T., Toffaletti, D., Cox, G.M., Miller, J.L., Perfect, J.R., 2006. Characterization and regulation of the trehalose synthesis pathway and its importance in the pathogenicity of *Cryptococcus neoformans*. Infect. Immun. 74 (10), 5877–5887. https://doi.org/10.1128/IAI.00624-06.

Poullet, J.B., Sima, D.M., Simonetti, A.W., De Neuter, B., Vanhamme, L., Lemmerling, P., Van Huffel, S., 2007. An automated quantification of short echo time MRS spectra in

an open source software environment: AQSES. NMR Biomed. 20, 493–504. https://doi.org/10.1002/nbm.1112.
Rajasingham, R., Smith, R.M., Park, B.J., Jarvis, J.N., Govender, N.P., Chiller, T.M., Denning, D.W., Loyse, A., Boulware, D.R., 2017. Global burden of disease of HIV-associated cryptococcal meningitis: an updated analysis. Lancet Infect. Dis. 17 (8), 873–881. https://doi.org/10.1016/S1473-3099(17)30243-8.
Riva, M., Wouters, R., Weerasekera, A., Belderbos, S., Nittner, D., Thal, D.R., Baert, T., Giovannoni, R., Gsell, W., Himmelreich, U., Van Ranst, M., Coosemans, A., 2019. CT-2A neurospheres-derived high-grade glioma in mice: a new model to address tumor stem cells and immunosuppression. Biol. Open 8, 044552. https://doi.org/10.1242/bio.044552.
Roussel, T., Rosenberg, J.T., Grant, S.C., Frydman, L., 2018. Brain investigations of rodent disease models by chemical exchange saturation transfer at 21.1 T. NMR Biomed. 31 (11), e3995. https://doi.org/10.1002/nbm.3995.
Santander, X.A., Gutiérrez-González, R., Cotúa, C., Tejerina, E., Rodríguez, G.-B., 2019. Intraventricular cryptococcoma mimicking a neoplastic lesion in an immunocompetent patient with hydrocephalus: a case report. Surg. Neurol. Int. 10, 115. https://doi.org/10.25259/sni-104-2019.
Santos, J.R.A., Ribeiro, N.Q., Bastos, R.W., Holanda, R.A., Silva, L.C., Queiroz, E.R., Santos, D.A., 2017. High-dose fluconazole in combination with amphotericin B is more efficient than monotherapy in murine model of cryptococcosis. Sci. Rep. 7, 4661. https://doi.org/10.1038/s41598-017-04588-7.
Schneider, C.A., Rasband, W.S., Eliceiri, K.W., 2012. NIH Image to ImageJ: 25 years of image analysis. Nat. Methods 9 (7), 671–675. https://doi.org/10.1038/nmeth.2089.
Schwartz, S., Kontoyiannis, D.P., Harrison, T., Ruhnke, M., 2018. Advances in the diagnosis and treatment of fungal infections of the CNS. Lancet Neurol. 17 (4), 362–372. https://doi.org/10.1016/S1474-4422(18)30030-9.
Singh, N., Lortholary, O., Dromer, F., Alexander, B.D., Gupta, K.L., John, G.T., del Busto, R., Klintmalm, G.B., Somani, J., Lyon, G.M., Pursell, K., Stosor, V., Muñoz, P., Limaye, A.P., Kalil, A.C., Pruett, T.L., Garcia-Diaz, J., Humar, A., Houston, S., House, A.A., Wray, D., Orloff, S., Dowdy, L.A., Fisher, R.A., Heitman, J., Wagener, M. M., Husain, S., 2008. Central nervous system cryptococcosis in solid organ transplant recipients: clinical relevance of abnormal neuroimaging findings. Transplantation 86, 647–651. https://doi.org/10.1097/TP.0b013e3181814e76.
Stefan, D., Cesare, F.D., Andrasescu, A., Popa, E., Lazariev, A., Vescovo, E., Strbak, O., Williams, S., Starcuk, Z., Cabanas, M., van Ormondt, D., Graveron-Demilly, D., 2009. Quantitation of magnetic resonance spectroscopy signals: the jMRUI software package. Meas. Sci. Technol. 20 (10), 104035. https://doi.org/10.1088/0957-0233/20/10/104035.
Sun, P.Z., Farrar, C.T., Sorensen, A.G., 2007. Correction for artifacts induced by B0 and B1 field inhomogeneities in pH-sensitive chemical exchange saturation transfer (CEST) imaging. Magn. Reson. Med. 58 (6), 1207–1215. https://doi.org/10.1002/(ISSN)1522-259410.1002/mrm.v58:610.1002/mrm.21398.
Tkáč, I., Henry, P.-G., Andersen, P., Keene, C.D., Low, W.C., Gruetter, R., 2004. Highly resolved *in vivo* 1 H NMR spectroscopy of the mouse brain at 9.4 T. Magn. Reson. Med. 52 (3), 478–484. https://doi.org/10.1002/mrm.20184.
Ulett, K.B., Cockburn, J.W.J., Jeffree, R., Woods, M.L., 2017. Cerebral cryptococcoma mimicking glioblastoma. BMJ Case Rep. 2017, bcr2016218824. DOI:10.1136/bcr-2016-218824.
van Zijl, P.C.M., Yadav, N.N., 2011. Chemical exchange saturation transfer (CEST): what is in a name and what isn't? Magn. Reson. Med. 65 (4), 927–948. https://doi.org/10.1002/mrm.22761.
van Zijl, P.C.M., Jones, C.K., Ren, J., Malloy, C.R., Sherry, A.D., 2007. MRI detection of glycogen *in vivo* by using chemical exchange saturation transfer imaging (glycoCEST). Proc. Natl. Acad. Sci. 104 (11), 4359–4364. https://doi.org/10.1073/pnas.0700281104.
Vanherp, L., Ristani, A., Poelmans, J., Hillen, A., Lagrou, K., Janbon, G., Brock, M., Himmelreich, U., Vande Velde, G., 2019. Sensitive bioluminescence imaging of fungal dissemination to the brain in mouse models of cryptococcosis. Dis. Model. Mech. 12, dmm039123. https://doi.org/10.1242/dmm.039123.
Vanherp, L., Poelmans, J., Hillen, A., Janbon, G., Brock, M., Lagrou, K., Vande Velde, G., Himmelreich, U., 2020. The added value of longitudinal imaging for preclinical in vivo efficacy testing of therapeutic compounds against cerebral cryptococcosis. Antimicrob. Agents Chemother. 64 (7) https://doi.org/10.1128/AAC.00070-20.
Vanherp, L., Poelmans, J., Weerasekera, A., Hillen, A., Croitor-Sava, A.R., Sorrell, T.C., Lagrou, K., Vande Velde, G., Himmelreich, U., 2021. Trehalose as quantitative biomarker for in vivo diagnosis and treatment follow-up in cryptococcomas. Transl. Res. 230, 111–122. https://doi.org/10.1016/j.trsl.2020.11.001.
Voelz, K., Johnston, S.A., Rutherford, J.C., May, R.C., Nielsen, K., 2010. Automated analysis of cryptococcal macrophage parasitism using GFP-tagged cryptococci. PLoS One 5 (12), e15968. https://doi.org/10.1371/journal.pone.0015968.
Walker-Samuel, S., Ramasawmy, R., Torrealdea, F., Rega, M., Rajkumar, V., Johnson, S. P., Richardson, S., Gonçalves, M., Parkes, H.G., Årstad, E., Thomas, D.L., Pedley, R. B., Lythgoe, M.F., Golay, X., 2013. *In vivo* imaging of glucose uptake and metabolism in tumors. Nat. Med. 19 (8), 1067–1072. https://doi.org/10.1038/nm.3252.
Wang, J., Weygand, J., Hwang, K.P., Mohamed, A.S.R., Ding, Y., Fuller, C.D., Lai, S.Y., Frank, S.J., Zhou, J., 2016. Magnetic resonance imaging of glucose uptake and metabolism in patients with head and neck cancer. Sci. Rep. 6, 1–7. https://doi.org/10.1038/srep30618.
Ward, K.M., Aletras, A.H., Balaban, R.S., 2000. A new class of contrast agents for MRI based on proton chemical exchange dependent saturation transfer (CEST). J. Magn. Reson. 143 (1), 79–87. https://doi.org/10.1006/jmre.1999.1956.
Windschuh, J., Zaiss, M., Meissner, J.E., Paech, D., Radbruch, A., Ladd, M.E., Bachert, P., 2015. Correction of B1-inhomogeneities for relaxation-compensated CEST imaging at 7T. NMR Biomed. 28, 529–537. https://doi.org/10.1002/nbm.3283.
Xu, X., Sehgal, A.A., Yadav, N.N., Laterra, J., Blair, L., Blakeley, J., Seidemo, A., Coughlin, J.M., Pomper, M.G., Knutsson, L., Zijl, P.C.M., 2020. D-glucose weighted chemical exchange saturation transfer (glucoCEST)-based dynamic glucose enhanced (DGE) MRI at 3T: early experience in healthy volunteers and brain tumor patients. Magn. Reson. Med. 84, 247–262. https://doi.org/10.1002/mrm.28124.
Xu, J., Zaiss, M., Zu, Z., Li, H., Xie, J., Gochberg, D.F., Bachert, P., Gore, J.C., 2014. On the origins of chemical exchange saturation transfer (CEST) contrast in tumors at 9.4T. NMR Biomed. 27, 406–416. https://doi.org/10.1002/nbm.3075.
Yushkevich, P.A., Piven, J., Hazlett, H.C., Smith, R.G., Ho, S., Gee, J.C., Gerig, G., 2006. User-guided 3D active contour segmentation of anatomical structures: significantly improved efficiency and reliability. Neuroimage 31 (3), 1116–1128. https://doi.org/10.1016/j.neuroimage.2006.01.015.
Zhang, X.Y., Xie, J., Wang, F., Lin, E.C., Xu, J., Gochberg, D.F., Gore, J.C., Zu, Z., 2017. Assignment of the molecular origins of CEST signals at 2 ppm in rat brain. Magn. Reson. Med. 78, 881–887. https://doi.org/10.1002/mrm.26802.
Zhou, J., Payen, J.-F., Wilson, D.A., Traystman, R.J., van Zijl, P.C.M., 2003. Using the amide proton signals of intracellular proteins and peptides to detect pH effects in MRI. Nat. Med. 9 (8), 1085–1090. https://doi.org/10.1038/nm907.
Zhou, J., Heo, H.-Y., Knutsson, L., van Zijl, P.C.M., Jiang, S., 2019. APT-weighted MRI: techniques, current neuro applications, and challenging issues. J. Magn. Reson. Imaging 50 (2), 347–364. https://doi.org/10.1002/jmri.v50.210.1002/jmri.26645.
Zhou, I.Y., Wang, E., Cheung, J.S., Zhang, X., Fulci, G., Sun, P.Z., 2017. Quantitative chemical exchange saturation transfer (CEST) MRI of glioma using Image Downsampling Expedited Adaptive Least-squares (IDEAL) fitting. Sci. Rep. 7, 1–10. https://doi.org/10.1038/s41598-017-00167-y.